Wavenumber illumination analysis validation: which elastic anisotropic parameters can we resolve?

Vladimir Kazei, Dmitry Kabanov & Tariq Alkhalifah, KAUST

SUMMARY

Vertical fractures are often embedded into a finely layered medium, which leads to an effective medium with orthorhombic anisotropy. Ten independent parameters are necessary to completely characterize such a medium, including density and excluding rotations. Through wavenumber illumination analysis, it has been shown that only six of these parameters can be reliably inverted from $P-P$ scattered energy. Here, we demonstrate that with the addition of converted waves, nine parameters can principally be recovered. We also demonstrate that the one-dimensional null space is along a linear combination of the shear-wave dimensionless parameters, γ_1 and γ_2, or a linear combination of the elastic coefficients C_{12} and C_{66} parameters. This null space can be captured by the Thomsen γ parameter if it is introduced into the parameterization. Finally and most importantly, there is still a lot of skepticism around the applicability of multiparameter model wavenumber illumination analysis, so we validate the radiation patterns using finite-difference modeling code. We find that theoretical scattering patterns are in good agreement with numerically modeled wavefields scattered from thin layers. The latter is a step towards applications of similar analysis, initially in the framework of time-lapse monitoring of the reservoirs, where the perturbations of parameters are generally small.

INTRODUCTION

Hydrocarbon reservoirs, naturally, have stratigraphic horizontal layering and are pre-stressed in the vertical direction. These conditions lead to natural systems of vertical fractures and the elastic medium at the scale of seismic exploration wavelengths acts like an orthorhombic one (Schoenberg and Helbig, 1997; Ivanov and Stovas, 2016). *P*-waves are the primary source of information in seismic exploration. Unfortunately, neither traveltimes of *P*-waves (Tsvankin, 1997) nor their amplitudes (Kazei and Alkhalifah, 2018b) can reveal the full set of orthorhombic parameters. Simultaneous Dix-type inversion of moveouts of *P*-waves with converted waves leads to the full recovery of the nine elastic constants (Grechka et al., 1999). Kinematic features of *P*-, *S*- (Stovas, 2015, 2017) and converted waves in general orthorhombic media are rather complicated, which leads us towards full-waveform inversion in orthorhombic media (de Hoop et al., 1999; Köhn et al., 2015; Oh and Alkhalifah, 2016). Recently, wavenumber illumination analysis (Devaney, 1984; Mora, 1989; Kazei et al., 2013) was adopted to reveal the number of anisotropic parameters resolvable from different types of data (Podgornova et al., 2015; Kazei and Alkhalifah, 2018b; Podgornova et al., 2018; Kazei and Alkhalifah, 2019). Here, we extend the scattering radiation pattern analysis in the wavenumber domain and compare several parameterizations in it. Namely, we look at scattering in the wavenumber domain by perturbations of single parameters in three parameterizations. These parameterizations are the classic elastic stiffnesses in the Voigt notation; the Tsvankin (1997) extension of the Thomsen (1986) parameters; and the recently introduced hierarchical parametrization (Masmoudi and Alkhalifah, 2016; Oh and Alkhalifah, 2016; Kazei and Alkhalifah, 2018b, 2019) based on the Alkhalifah and Tsvankin (1995) parameterization. Finally, we validate the analysis by comparing the results to the snapshots of scattered wavefields from weakly anisotropic fine layers embedded into a homogeneous isotropic background.

WAVENUMBER ILLUMINATION THEORY

The Born approximation for the scattered wavefield $\delta\mathbf{U}$ for a source located at $\mathbf{x}_s$ and a receiver at $\mathbf{x}_g$ for a perturbation in the density $\delta\rho(\mathbf{x})$ and the stiffness tensor $\delta c_{ijkl}(\mathbf{x})$ can be expressed as follows (Hudson and Heritage, 1981):

$$\delta\mathbf{U}(\mathbf{x}_s,\mathbf{x}_\mathbf{g},\omega) = \int_{-\infty}^{+\infty}\int_{-\infty}^{+\infty}\int_{-\infty}^{+\infty}(\omega^2\delta\rho(\mathbf{x})\mathbf{u}^0\cdot\mathbf{G} - \tag{1}$$

$$\nabla\mathbf{u}^0 : \delta\mathbf{c}(\mathbf{x}) : \nabla\mathbf{G}(\mathbf{x}_g,\mathbf{x}))\,\mathrm{d}\mathbf{x}, \tag{2}$$

where $\mathbf{u}^0$ is the incident wavefield, $\mathbf{G}$ is the Green's tensor and ω is the angular frequency. The far-field plane wave approximation of the Green's tensor in equation 1, consisting of *P*-, *SV*-, and *SH*-waves (Snieder, 2002; Podgornova et al., 2015), is used for our analysis. Different components of the Green's function are approximated locally by plane waves, as follows:

$$\mathbf{G} = \mathbf{G}_P + \mathbf{G}_{SV} + \mathbf{G}_{SH},\ \mathbf{G}_P \propto e^{i\frac{\omega}{v_p}\mathbf{g}\cdot(\mathbf{x}-\mathbf{x}_g)}\mathbf{gg}, \tag{3}$$

$$\mathbf{g} = \frac{\mathbf{x}-\mathbf{x}_g}{|\mathbf{x}-\mathbf{x}_g|}, (\mathbf{gg})_{ik} \equiv g_i g_k, \tag{4}$$

The first component $\mathbf{G}_P$, is approximated by a local plane *P*-wave. The second component represents shear waves polarized in the vertical plane containing source and receiver directions and the third component of the Green's tensor is the *SH*-wave polarized along $\mathbf{g}_\phi$, which is the horizontal component of the shear wave:

$$\mathbf{G}_{SV} \propto e^{i\frac{\omega}{v_s}\mathbf{g}\cdot(\mathbf{x}-\mathbf{x}_g)}\mathbf{g}_\theta\mathbf{g}_\theta, \quad \text{where } \mathbf{g}_\theta = \left(\frac{\mathbf{g}\times\mathbf{e}_z}{|\mathbf{g}\times\mathbf{e}_z|}\times\mathbf{e}_z\right), \tag{5}$$

$$\mathbf{G}_{SH} \propto e^{i\frac{\omega}{v_s}\mathbf{g}\cdot(\mathbf{x}-\mathbf{x}_g)}\mathbf{g}_\phi\mathbf{g}_\phi, \qquad \text{where } \mathbf{g}_\phi = \left(\frac{\mathbf{g}\times\mathbf{e}_z}{|\mathbf{g}\times\mathbf{e}_z|}\right). \tag{6}$$

P–*P* scattered waves

The amplitude of the scattered *P*-wave is proportional to a linear combination of Fourier transforms of the perturbed parameters (Kazei and Alkhalifah, 2017):

$$\delta U_{PP}(\mathbf{s},\mathbf{g},\omega) \propto \mathbf{s}\cdot\mathbf{g}\,\delta\hat{\rho}(\mathbf{K}_{PP}) + \mathbf{ss}\ \delta\hat{\mathbf{c}}(\mathbf{K}_{PP})\mathbf{gg}, \tag{7}$$

$$\mathbf{K}_{PP} = \frac{\omega}{V_p}(\mathbf{s}+\mathbf{g}). \tag{8}$$

Here, vectors $\mathbf{s}$ and $\mathbf{g}$ point towards the source and the receiver, respectively (Fig. 1(a)). For the case of a point scatterer $\delta\hat{\rho}(\mathbf{K}) = \text{const}, \delta\hat{\mathbf{c}}_{ijkl}(\mathbf{K}) = \text{const}$, equation (7) provides the radiation pattern or scattering function of these scatterers (Eaton and Stewart, 1994; de Hoop et al., 1999; Shaw and Sen,

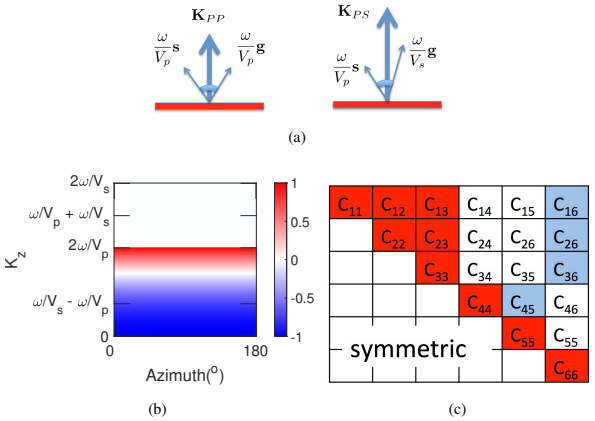

Figure 1: (a) Wavenumbers illuminated by different types of scattered waves. P-S waves illuminate higher wavenumbers and S-S waves the highest. (b) Reflection-based radiation pattern for density and scattered P-P waves in the C_{ij},ρ parameterization. Density does not scatter at intermediate angles in this parameterization and the middle wavenumbers in the $P-P$ scattering range are missing.(c) Orthorhombic parameters in the Voigt notation – red. Rotated orthorhombic medium can also include parameters in blue, they are excluded from analysis.

2004). Kazei and Alkhalifah (2018b) looked at *P–P* scattering using arbitrary vertical wavenumbers in the perturbation, which lead to the following relations (the vertical axis is labeled 3, while the azimuth, ϕ, is measured from the x_1 axis):

$$\delta U_{PP}(k_z,\phi,\omega(k_z,K_z)) \propto \mathbf{A}^T_{PP}(k_z,\phi)(\delta\rho(K_z),\delta\mathbf{c}(K_z))^T, \quad (9)$$

$$\text{or } \delta\mathbf{U}_{PP}(K_z) \propto \mathbb{A}_{PP}\delta\mathbf{m}(K_z). \quad (10)$$

Vector $\mathbf{A}(k_z,\phi)$ here is essentially a set of reflection-based radiation patterns remapped into the normalized wavenumber domain (Fig. 1(b)). Only *six* independent parameters can be inverted from *P–P* waves in the linearized anisotropic orthorhombic approximation (Kazei and Alkhalifah, 2018b, 2019). Here, we extend the approach to converted waves to investigate the benefits of a joint inversion.

Converted waves

Reflection-based radiation patterns are aimed at mimicking the behavior of the amplitudes of reflections from horizontal reflectors, yet converted waves are a special case. Unlike monotypic waves, where non-zero vertical wavenumbers are illuminated by reflections and only zero purely vertical wavenumbers are recoverable from pure transmissions. The wavenumber coverage of converted waves is produced by both converted transmissions and converted reflections (Podgornova et al., 2018; Kazei and Alkhalifah, 2018a, 2019). Combining (1) and (3), we derive an expression for the amplitude of scattered *P–SV* and *P–SH* waves:

$$\delta U_{PSV} \propto \frac{1}{\varkappa^3}\int_V e^{i\mathbf{K}_{PS}\cdot\mathbf{x}}(\mathbf{s}\cdot\mathbf{g}_\theta\delta\rho - \mathbf{ss}:\delta\mathbf{c}:\mathbf{gg}_\theta)\,\mathrm{d}\mathbf{x}, \quad (11)$$

$$\mathbf{K}_{PS} = \frac{\omega}{v_p}\mathbf{s} + \frac{\omega}{v_s}\mathbf{g},\ \varkappa = \frac{v_s}{v_p}, \quad (12)$$

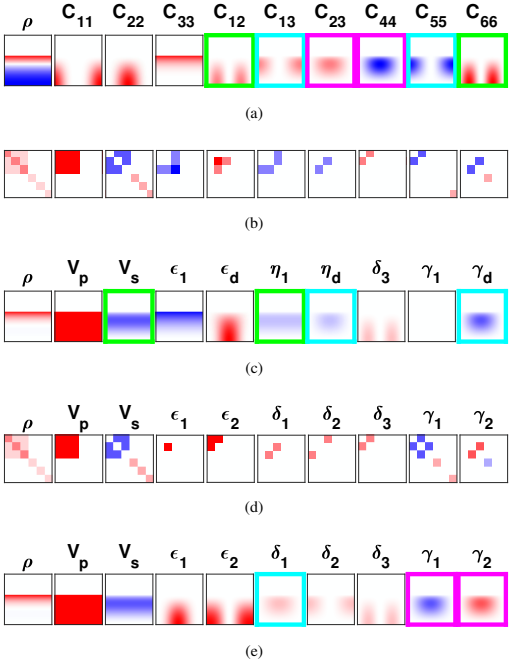

Figure 2: (a) Spectral sensitivities to vertical wavenumbers for $P-P$ scattering in C_{ij},ρ parameterization. Sensitivity to all monoclinic parameters is non zero if we start from isotropic background. Elements establishing similar scattering have the same color frames. C_{13} is very similar to C_{55}, C_{12} - to C_{66}, C_{23} - to C_{44}. High wavenumbers for density resemble those for C_{33}.(b) Partial derivatives of the C_{ij} parameters w.r.t. hierarchical parameters according to the map Fig. 1(c). (c) Wavenumber illumination patterns for different hierarchical parameters. (d) and (e) same as (b) and (c) respectively but for Tsvankin-Thomsen parameters ($V_p/V_s=\sqrt{3}$).

$$\delta U_{PSH} \propto \frac{1}{\varkappa^3}\int_V e^{i\mathbf{K}_{PS}\cdot\mathbf{x}}(\mathbf{s}\cdot\mathbf{g}_\phi\delta\rho - \mathbf{ss}:\delta\mathbf{c}:\mathbf{gg}_\phi)\,\mathrm{d}\mathbf{x} = \quad (13)$$

$$\mathbf{s}\cdot\mathbf{g}_\phi\delta\hat{\rho}(\mathbf{K}_{PS}) - \mathbf{ss}:\delta\hat{\mathbf{c}}(\mathbf{K}_{PS}):\mathbf{gg}_\phi. \quad (14)$$

Similarly to *P–P* scattered waves, monochromatic converted waves illuminate a single wavenumber $\mathbf{K}_{PS}$ for a single scattering angle, Fig. 1(a) for *P–SV* (Fig. 3(a), Fig. 3(b)) and for *P–SH* waves $\mathbf{A}_{PSH}$ (Fig. 4(a), Fig. 4(b)) can be constructed.

VALIDATION OF RADIATION PATTERNS

We introduce a thin layer of 50 meters thickness into an isotropic medium and illuminate it with an explosive source. We place a single source at depth 960 m and introduce the thin layer at depth 1500 m. The source we use is a Ricker wavelet with the central frequency of 5 Hz. The reflections caused by small anisotropic perturbations of elastic parameters inside the layer are supposed to validate our radiation patterns. In order to compare with the radiation patterns of *P*-waves, we extract the divergence of the wavefield. To analyse *P–SH* waves, we look at the vertical component of the curl of the wavefield. Fig. 5 shows several representative cases of scattering on thin layers with the perturbations of single parameters in Tsvankin-Thomsen parametrization.

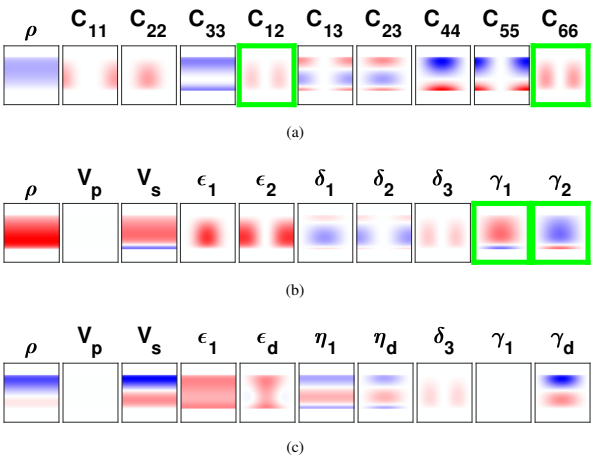

Figure 3: Same as Fig. 2(a), Fig. 2(e), and Fig. 2(c) respectively but for $P-SV$ waves.

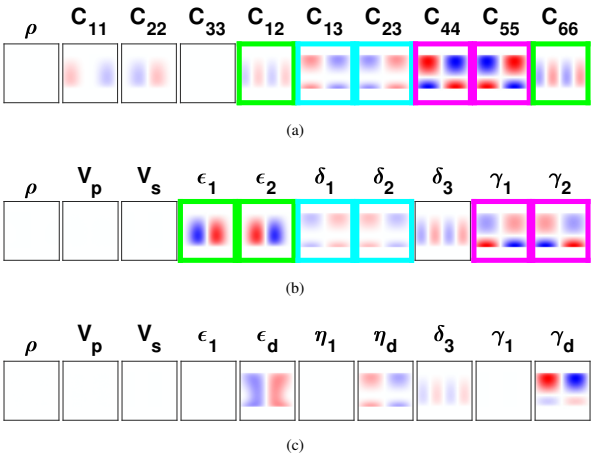

Figure 4: Same as Fig. 3 but for $P-SH$ scattering. Hierarchical parameterization shows that $P-SH$ type of scattering does not happen in VTI media due to simple symmetry restrictions, however, it is directly visible that some tradeoff

Data:	$P-P$	$P-SH$	$P-SV$	P-All
0 VTI:	$\boldsymbol{\gamma}_1+\boldsymbol{\gamma}_2$	all	$\mathbf{V}_p$	$\boldsymbol{\gamma}_1+\boldsymbol{\gamma}_2$
	$(\mathbf{C}_{11}+\mathbf{C}_{12}+$ $+\mathbf{C}_{22}-\mathbf{C}_{33}+\rho$	–	$\boldsymbol{\gamma}_1+\boldsymbol{\gamma}_2$	–
	$(2\mathbf{C}_{23}+\mathbf{C}_{44}+$ $2\mathbf{C}_{13}+\mathbf{C}_{55})$	–	–	–
0 ORT:	$2\mathbf{C}_{23}+\mathbf{C}_{44}$	–	–	–
# par.:	6	4	8	9

Table 1: Principally irresolvable linear combinations of orthorhombic parameters, number of resolvable parameters, and possible set of parameters that could be resolved from the C_{ij},ρ parameters for different types of scattering recorded under perfect illumination.

DISCUSSION AND CONCLUSIONS

P–SV scattering happens for all nine elastic orthorhombic parameters and density in the parametrization by the Voigt parameters. In the Tsvankin–Thomsen parametrization, V_p perturbations do not scatter converted waves and the tradeoff between γ_1 and γ_2 is apparent in Fig. 3(b). Hierarchical parametrization, on the other hand (Oh and Alkhalifah, 2016; Kazei and Alkhalifah, 2019), includes two non-scattering parameters γ_1 and V_p (Fig. 3(c)). The SVD analysis applied to the matrix $\mathbb{A}_{PSV}$ shows that there are only two zero singular values and hence the rest of the parameters can theoretically be resolved.

P–SH scattering does not exist in VTI media, and therefore, perturbations in the density or C_{33} in the $C_{ij},\rho-$ (Voigt) parameterization do not scatter (Fig. 4(a)). For the same reason, parameters with VTI type of symmetry do not scatter in the hierarchical parameterization (Fig. 4(b)). Applying SVD analysis to the matrix $\mathbb{A}_{PSH}$, we show that the other four orthorhombic parameters can be retrieved from this type of waves.

Combining information from converted and $P-P$ waves
In order to decouple anisotropic parameters for a given spatial wavenumber $\mathbf{K}$, we need to have this wavenumber illuminated from different scattering angles, modes and/or azimuths (different frequencies). $\mathbf{K}_{PS}$ wavenumber is larger than $\mathbf{K}_{PP}$ for the same scattering angle (Fig. 1(a)), and therefore, information from the same scattering angles is mapped to different resolution scales. The latter means that in order to understand how many or which parameters can be decoupled/inverted at a given resolution we need to look at the spectral sensitivities rather than the standard reflection-based radiation patterns.

In the current study, we consider the perfect illumination case, we only combine patterns in the wavenumber domain, and thus, highlight invertible parameters from different wave types and their combinations in Table 1. In the meantime, in realistic cases with limited aperture and frequency band, we can deduce the limitations in parameter resolution and inversion by remapping portions of the scattering response to the wavenumber component and we will share those insights in the presentation. In perfect illumination, *P–SV* waves alone can principally allow for the reconstruction of eight parameters, everything except V_p and γ_1 (Kazei and Alkhalifah, 2018a, 2019). Together with *P*-waves, they allow to invert everything except γ_1 parameter in the hierarchical parameterization or $\boldsymbol{\gamma}_1+\boldsymbol{\gamma}_2$ in Tsvankin-Thomsen parameterization.

ACKNOWLEDGMENTS

Vladimir Kazei is grateful to Jean Virieux and David Lumley for discussions on Born approximation applicability in the framework of time-lapse full-waveform inversion. We thank King Abdullah University of Science and Technology for support of this study. The codes for the radiation pattern analysis and the wavefield snapshots generation are available at **https://github.com/vkazei/ScatteringAtlas** and **https://github.com/swag-kaust/ASOFI3D** respectively.

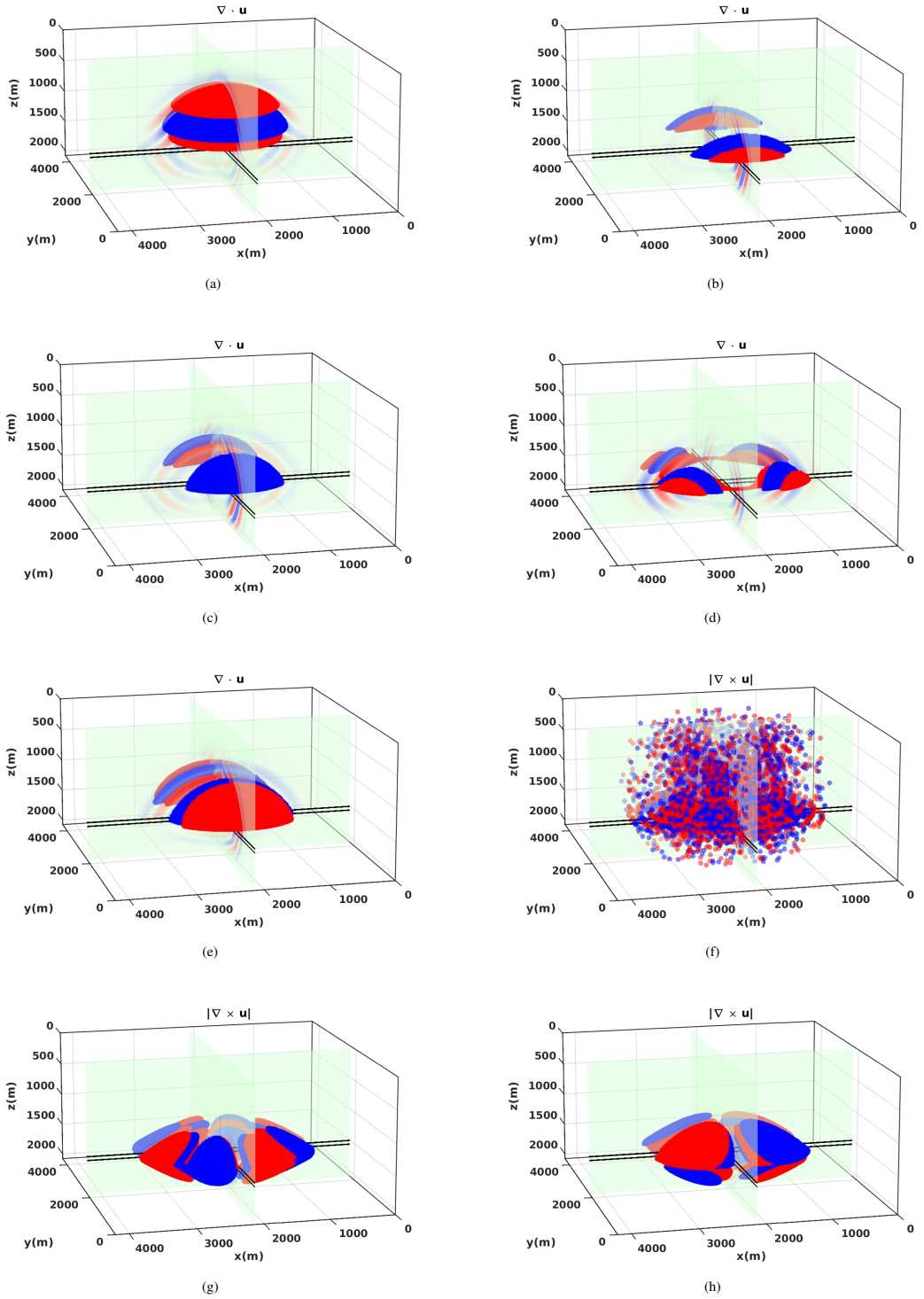

Figure 5: Scattering by different perturbations of single parameters in Tsvankin-Thomsen parameterization. Divergence (P-wave (a)-(e), compare with Fig. 2(e)) and vertical component of the curl (SH-wave (f)-(h), compare with Fig. 4(b)) of the scattered wavefield is displayed. Subplot – perturbation list: (a)-ρ, backscattering – high wavenumbers; (b)-ε_1, scatters in Y-Z, but not in X-Z plane; (c)-δ_1, opposite to (b), middle angles; (d)-δ_3, doesn't scatter in symmetry planes; (e)-γ_2, looks different from $delta_1$, but in fact the polarity is the same if we count cycles in the plane of symmetry; (f)-ρ, no scattering in $P-SH$ mode; (g)-δ_3, four cycles in the whole azimuth; (h)-γ_2, switch of polarity between transmission and reflection of converted waves. All amplitudes are normalized on absolute maximum in each scattering type.

REFERENCES

Alkhalifah, T., and I. Tsvankin, 1995, Velocity analysis for transversely isotropic media: GEOPHYSICS, **60**, 1550–1566.

de Hoop, M. V., C. Spencer, and R. Burridge, 1999, The resolving power of seismic amplitude data: An anisotropic inversion/migration approach: Geophysics, **64**, 852–873.

Devaney, A. J., 1984, Geophysical diffraction tomography: IEEE Transactions on Geoscience and Remote Sensing, **GE-22**, 3–13.

Eaton, D. W. S., and R. R. Stewart, 1994, Migration/inversion for transversely isotropic elastic media: Geophysical Journal International, **119**, 667–683.

Grechka, V., S. Theophanis, and I. Tsvankin, 1999, Joint inversion of p- and ps-waves in orthorhombic media: Theory and a physical modeling study: GEOPHYSICS, **64**, 146–161.

Hudson, J., and J. Heritage, 1981, The use of the born approximation in seismic scattering problems: Geophysical Journal International, **66**, 221–240.

Ivanov, Y., and A. Stovas, 2016, Upscaling in orthorhombic media: Behavior of elastic parameters in heterogeneous fractured earth: GEOPHYSICS, **81**, C113–C126.

Kazei, V., and T. Alkhalifah, 2017, On the resolution of inversion for orthorhombic anisotropy: Presented at the 79th EAGE Conference and Exhibition 2017.

———, 2018a, Resolving orthorhombic anisotropy with the addition of ps conversions: Presented at the 80th EAGE Conference and Exhibition 2018.

———, 2018b, Waveform inversion for orthorhombic anisotropy with P-waves: Feasibility & resolution: Geophysical Journal International, ggy034.

———, 2019, Scattering Radiation Pattern Atlas: What anisotropic elastic properties can body waves resolve?: JGR Solid Earth (submitted).

Kazei, V., V. Troyan, B. Kashtan, and W. Mulder, 2013, On the role of reflections, refractions and diving waves in full-waveform inversion: Geophysical Prospecting, **61**, 1252–1263.

Köhn, D., O. Hellwig, D. De Nil, and W. Rabbel, 2015, Waveform inversion in triclinic anisotropic mediaa resolution study: Geophysical Journal International, **201**, 1642–1656.

Masmoudi, N., and T. Alkhalifah, 2016, A new parameterization for waveform inversion in acoustic orthorhombic media: Geophysics, **81**, R157–R171.

Mora, P., 1989, Inversion = migration + tomography: Geophysics, **54**, 1575–1586.

Oh, J.-W., and T. Alkhalifah, 2016, Elastic orthorhombic anisotropic parameter inversion: An analysis of parameterization: GEOPHYSICS, **81**, C279–C293.

Podgornova, O., S. Leaney, and L. Liang, 2018, Resolution of VTI anisotropy with elastic full-waveform inversion: Theory and basic numerical examples: Geophysical Journal International, ggy116–ggy116.

Podgornova, O., S. Leaney, L. Liang, et al., 2015, Analysis of resolution limits of vti anisotropy with full waveform inversion: Presented at the 2015 SEG Annual Meeting, Society of Exploration Geophysicists.

Schoenberg, M., and K. Helbig, 1997, Orthorhombic media: Modeling elastic wave behavior in a vertically fractured earth: Geophysics, **62**, 1954–1974.

Shaw, R. K., and M. K. Sen, 2004, Born integral, stationary phase and linearized reflection coefficients in weak anisotropic media: Geophysical Journal International, **158**, 225–238.

Snieder, R., 2002, Chapter 1.7.1 - general theory of elastic wave scattering, *in* Scattering: Academic Press, 528 – 542.

Stovas, A., 2015, Azimuthally dependent kinematic properties of orthorhombic media: GEOPHYSICS, **80**, C107–C122.

———, 2017, Kinematic parameters of pure- and converted-mode waves in elastic orthorhombic media: Geophysical Prospecting, **65**, 426–452.

Thomsen, L., 1986, Weak elastic anisotropy: GEOPHYSICS, **51**, 1954–1966.

Tsvankin, I., 1997, Anisotropic parameters and p-wave velocity for orthorhombic media: Geophysics, **62**, 1292–1309.